Highly Ordered Mesoporous Cobalt-Containing Oxides: Structure, Catalytic Properties, and Active Sites in Oxidation of Carbon Monoxide

Dong Gu,[†] Chun-Jiang Jia,*,[†,‡] Claudia Weidenthaler,[†] Hans-Josef Bongard,[†] Bernd Spliethoff,[†] Wolfgang Schmidt,[†] and Ferdi Schüth*,[†]

[†]Max-Planck-Institut für Kohlenforschung, Kaiser-Wilhelm-Platz 1, 45470 Mülheim an der Ruhr, Germany

[‡]Key Lab for Colloid and Interface Chemistry, School of Chemistry and Chemical Engineering, Shandong University, Jinan 250100, People's Republic of China

S *Supporting Information*

ABSTRACT: Co_3O_4 with a spinel structure is a very active oxide catalyst for the oxidation of CO. In such catalysts, octahedrally coordinated Co^{3+} is considered to be the active site, while tetrahedrally coordinated Co^{2+} is assumed to be basically inactive. In this study, a highly ordered mesoporous CoO has been prepared by H_2 reduction of nanocast Co_3O_4 at low temperature (250 °C). The as-prepared CoO material, which has a rock-salt structure with a single Co^{2+} octahedrally coordinated by lattice oxygen in $Fm\bar{3}m$ symmetry, exhibited unexpectedly high activity for CO oxidation. Careful investigation of the catalytic behavior of mesoporous CoO catalyst led to the conclusion that the oxidation of surface Co^{2+} to Co^{3+} causes the high activity. Other mesoporous spinels ($CuCo_2O_4$, $CoCr_2O_4$, and $CoFe_2O_4$) with different Co species substituted with non/low-active metal ions were also synthesized to investigate the catalytically active site of cobalt-based catalysts. The results show that not only is the octahedrally coordinated Co^{3+} highly active but also the octahedrally coordinated Co^{2+} species in $CoFe_2O_4$ with an inverse spinel structure shows some activity. These results suggest that the octahedrally coordinated Co^{2+} species is easily oxidized and shows high catalytic activity for CO oxidation.
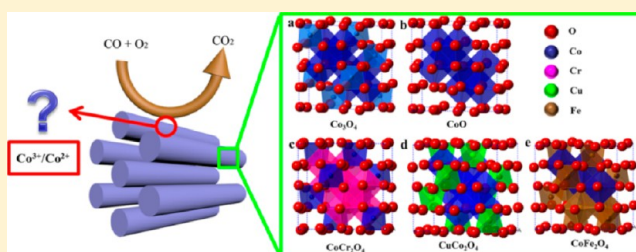
1. INTRODUCTION

Ordered mesoporous materials possess many attractive properties, such as high surface area, uniform and tunable pore sizes and shapes, and various structures and compositions, which make them suitable for applications in catalysis, adsorption, battery technology, sensing, and so on.[1−12] Moreover, the highly uniform nanopore system makes mesoporous materials ideal systems for designing structurally uniform materials as model catalysts for understanding the structural characteristics affecting the catalytic performance.[13,14]

Oxidation of carbon monoxide (CO) over solid catalysts is of great interest, not only due to its relevance in practical applications, such as in CO removal from the hydrogen feed of polymer−electrolyte−membrane fuel cells (PEMFC),[15,16] automotive exhaust gas treatment,[17,18] air cleaning,[19] and sensing,[20] but also due to its importance as a model reaction for the understanding of catalytic mechanisms. Co_3O_4 is one of the most active nonprecious metal catalysts for low-temperature CO oxidation. Xie et al.[21] synthesized Co_3O_4 nanorods with predominantly exposed {110} faces, which show very high activity for CO oxidation at −77 °C. This study revealed the importance of the face-selective properties of Co_3O_4 catalysts.[22] However, similarly high activity has also been reported for other Co_3O_4 systems, where the predominance of specific faces

is less obvious,[23] indicating that the complexity in surface structure of the catalyst makes it very difficult to precisely identify the active sites for CO oxidation. On the other hand, it is also questionable to what extent a single crystal surface reflects the surface structure of the real catalysts under reaction conditions.[24]

Co_3O_4 has a spinel structure, containing Co^{3+} on octahedral coordination sites and Co^{2+} on tetrahedral coordination sites. CoO contains exclusively Co^{2+} species in octahedral coordination and could thus be an ideal system for the identification of active sites for CO oxidation over Co-based catalysts. In both the spinel and the rock-salt structure, the oxygen sublattice forms a face-centered-cubic (fcc) structure, with ∼5% higher $O^{2−}−O^{2−}$ packing distance in the rock-salt structure than in the spinel structure.[24−26] All octahedral sites are filled in the rock-salt structure, but only half are filled in the spinel structure. The tetrahedral sites, which are completely unoccupied in the rock-salt structure, are partially filled to one-eighth occupancy in the spinel structure. In addition to CoO, different spinels with specific cobalt occupancies, such as $CuCo_2O_4$, $CoCr_2O_4$, and $CoFe_2O_4$ (inverse spinel structure with Co^{2+} octahedrally

coordinated), are also very interesting systems, which allow studies on the influence of charge and coordination state of cobalt on catalytic performance.

However, in order to be comparable, also the synthetic pathways have to be comparable, since catalyst preparation methods have a strong influence on the catalytic activities.[21,23] Nanocasting is a powerful method for preparing high surface area, nanosized, and crystalline catalysts.[9,27,28] In addition, mesoporous materials synthesized by the nanocasting method can be controlled to have similar structural and textural parameters, which makes them comparable with respect to their catalytic activities. Nanosized CoO particles hitherto could only be prepared by solvothermal methods at critical conditions, and their surface protection ligands always lead to contaminated surfaces.[29,30] Our group has successfully synthesized highly ordered mesoporous Co_3O_4 with controllable architectures[31] and proven that these materials are active for CO oxidation at low temperatures.[32] Such Co_3O_4 materials were also successfully transformed into CoO in a pseudomorphic manner by glycerol reduction.[33] However, formation of carbonaceous residues, which would affect catalytic performance, on the surface in this process cannot be excluded, and the coke is very difficult to remove due to possible reoxidation of CoO. Thus, in order to obtain directly comparable Co_3O_4 and CoO, alternative synthetic pathways are required.

In the following, we report the successful preparation of a series of cobalt-based catalysts (Co_3O_4, CoO, $CuCo_2O_4$, $CoCr_2O_4$, and $CoFe_2O_4$, Table 1) with similar structures and

Table 1. Mesoporous Metal Oxides with Different Cobalt Species[a]

sample	tetrahedral coordination	octahedral coordination
Co_3O_4	Co^{2+}	Co^{3+}
CoO		Co^{2+}
$CuCo_2O_4$	Cu^{2+}	Co^{3+}
$CoCr_2O_4$	Co^{2+}	Cr^{3+}
$CoFe_2O_4$	Fe^{3+}	Co^{2+}, Fe^{3+}

[a]In all the materials, the oxygen sublattice is *fcc*. The cations are located in the voids of the oxygen sublattices.

crystallite sizes by using the same mesoporous silica as a hard template. CoO is obtained via pseudomorphic transformation from Co_3O_4 by a low-temperature reduction process with hydrogen, which avoids the problem of carbon deposition on the CoO surface. Studies of the catalytic performance with respect to the charge and coordination of the cobalt species then allow determination of the active species for CO oxidation in such catalysts.

2. EXPERIMENTAL SECTION

2.1. Catalyst Synthesis. Mesoporous silica SBA-15 was prepared under hydrothermal conditions at 110 °C for 24 h, according to established procedures.[2,34] Highly ordered mesoporous Co_3O_4 was prepared by the nanocasting method with SBA-15 as a hard template. The $Co(NO_3)_2 \cdot 6H_2O$ precursor was incorporated into the channels of mesoporous silica via an evaporation-assisted impregnation process.[27,35] The ratio of precursor to template was fixed to 2.0 g of nitrate per mL of silica pore volume. The subsequent decomposition of the precursor was carried out in a muffle oven at 600 °C for 5 h with a ramp rate of 1 °C·min⁻¹. Finally, the mesoporous silica hard template was leached out with hot NaOH solution (2 M, 100 mL, 70 °C). Mesoporous CoO was prepared by reducing the nanocast mesoporous Co_3O_4 in 4.5 vol % H_2 at 250 °C for 1.5 h (250 mg Co_3O_4, 30 mL·

min⁻¹). Other spinel oxides ($CuCo_2O_4$, $CoCr_2O_4$, and $CoFe_2O_4$) were prepared accordingly with appropriate amounts of the respective metal nitrates as precursors. The calcination temperatures for $CuCo_2O_4$, $CoCr_2O_4$, and $CoFe_2O_4$ were 350, 600, and 600 °C, respectively.

2.2. Characterization and Measurements. Powder X-ray diffraction (XRD) patterns were recorded on a Stoe STADI P $\theta-\theta$ diffractometer operating in reflection mode with Cu $K\alpha_{1,2}$ radiation and a secondary graphite monochromator. Nitrogen adsorption–desorption measurements were performed on a NOVA 3200e instrument at 77 K. Prior to the measurements, all samples were degassed under vacuum for at least 6 h at 150 °C. Brunauer–Emmett–Teller (BET) surface areas were calculated from the data in a relative pressure range from 0.05 to 0.20. By using the Barrett–Joyner–Halenda (BJH) algorithm, the pore volumes and pore size distributions were derived from the adsorption branches of the isotherms (normally desorption is recommended, but the desorption branches could be influenced by the tensile strength effect). High-resolution scanning electron microscope (HR-SEM) images and scanning transmission electron microscope (STEM) images were taken on a Hitachi S-5500 ultra-high-resolution cold field emission scanning microscope at an acceleration voltage of 30 kV. A Thermo Scientific NORAN System 7 X-ray Microanalysis unit was attached to the instrument. Transmission electron microscopy (TEM) images of the catalysts were recorded with a Hitachi H-7100 microscope at an acceleration voltage of 100 kV, and high-resolution transmission images (HR-TEM) with a Hitachi HF2000 microscope at an acceleration voltage of 200 kV. The HF2000 microscope was equipped with a cold field emission gun and a Noran energy dispersive X-ray (EDX) unit. X-ray photoelectron spectroscopy (XPS) measurements were performed with a Kratos HSi spectrometer with a hemispherical analyzer. The monochromatized Al X-ray source (E = 1486.6 eV) was operated at 15 kV and 15 mA. For narrow scans, an analyzer pass energy of 40 eV was applied. Hybrid mode was used as lens mode. The base pressure in the analysis chamber was 4×10^{-9} Torr. The binding energy scale was corrected for surface charging by use of the C 1s peak of contaminant carbon as reference at 284.5 eV. Temperature-programmed reduction (TPR) experiments were performed with an in-house-constructed system, equipped with a thermal conductivity detector (TCD) to measure H_2 consumption. A 30 mg sample was reduced with a 4.5 vol % H_2/N_2 mixture (30 mL·min⁻¹) by heating to 800 °C at a rate of 10 °C·min⁻¹. A CO-TPR experiment was performed in the same reactor in which the CO oxidation activities were tested. A 50 mg sample was reduced with a 1 vol % CO/N_2 gas mixture (50 mL·min⁻¹) by heating to 550 °C at a rate of 5 °C·min⁻¹.

Fourier transform infrared (FTIR) spectra of CO adsorption over CoO and Co_3O_4 were measured in a diffuse reflectance cell (Harrick system) equipped with CaF_2 windows on a Bruker Vertex 70 spectrometer using a mercury–cadmium–telluride (MCT) detector. After pretreatment of the catalysts (30 mg) in a gas flow of N_2 (30 mL·min⁻¹) at 300 °C, the reaction cell was cooled to 20 °C in the N_2 stream. Then a background spectrum was collected via 32 scans at 4 cm⁻¹ resolution. The catalyst was exposed to 2 vol % CO in N_2 (30 mL·min⁻¹), and diffuse reflectance Fourier transform (DRIFT) spectra were obtained by subtracting the background spectrum from subsequent spectra. The IR spectra for CO adsorption were recorded continuously for 30 min. Once CO gas was switched to a N_2 steam, also the corresponding IR spectra were recorded for 30 min, in order to follow the surface changes during the CO removal process.

2.3. Catalytic Testing. The catalytic activity of catalysts for CO oxidation was measured in a plug flow reactor with an inner diameter of 6 mm by use of defined amounts of catalyst (200 mg of catalyst, space velocity (SV) = 15 000 mL·h⁻¹·g_{cat}⁻¹, or 50 mg of catalyst, SV = 80 000 mL·h⁻¹·g_{cat}⁻¹, or 10 mg of catalyst, SV = 600 000 mL·h⁻¹·g_{cat}⁻¹) in a gas mixture of 1 vol % CO, 20 vol % O_2, and 79 vol % He (from Air Liquid, 99.997% purity, H_2O content ~3 ppm) or in a gas mixture of 2.140 vol % CO, 0.876 vol % O_2, and He balance at a flow rate of 35, 50, 67, or 100 mL·min⁻¹, respectively. Catalysts were pressed, crushed, and sieved to the 250–500 μm size range and diluted with 200 mg of quartz sand; in the reactor the mixture was supported on a quartz wool plug. The operation temperature was controlled with

a thermocouple and could be adjusted in the range −100 to 400 °C. Temperatures measured during the catalytic tests are always referred to the value measured with a second thermocouple placed in the catalyst bed. Before measurement, the catalysts were first activated *in situ* in the reaction gas or He or H_2 at 200 or 300 °C for 30 min. For the experiments under dry conditions, the entire feed passed through a molecular sieve trap cooled to −78 °C (2-propanol/dry ice bath) before going into the reactor.

For a typical light-off run, in which the temperature was ramped, the reactor was cooled to −50 °C prior to each experiment under a flow of He gas, which was then replaced by the reaction gas, after the base temperature had been reached. Then, the temperature was ramped with a rate of 2 °C·min^{-1} to the final temperature. The concentrations of CO_2 and CO were analyzed at the outlet of the reactor with nondispersive IR spectroscopy on two URAS 3E analyzers (Hartmann and Braun).

The titration experiments were carried out in the same reactor in which the CO oxidation activities were tested, with 50 mg of catalyst. The catalysts were pretreated in the reaction gas (1 vol % CO, 20 vol % O_2, and 79 vol % He) at 300 °C (150 or 200 °C in He for CoO to prevent the oxidation of CoO to Co_3O_4) for 10 min. Then the gas was switched to He to remove the O_2 from the reactor. After the reactor was cooled to the desired temperature and kept for 10 min, the catalysts were exposed to a stream of 1 vol % CO in N_2 (from Air Liquid, 99.997% purity, H_2O content ∼3 ppm) at a flow rate of 67 mL· min^{-1}. Online analysis was performed with nondispersive IR analyzers (URSA 3E), which allowed detection of CO and CO_2 in a nitrogen matrix without interference problems.

3. RESULTS AND DISCUSSION

3.1. Mesoporous CoO Catalyst. Mesoporous CoO was synthesized by reducing nanocast Co_3O_4 in 4.5 vol % H_2 at 250 °C. One should note that mesoporous Co_3O_4 was used not only as a precursor for the synthesis of CoO with the same architecture but also as reference catalyst. Mesoporous silica SBA-15 that was obtained with an aging temperature of 110 °C was selected as a hard template, since the pore volume and specific surface area of mesoporous silica templates change with aging temperature, and aging at 110 °C was found to be advantageous for the nanocasting process.[34−37] The obtained SBA-15 silica template with highly ordered mesostructure (Figure S1, Supporting Information) has a large pore volume (1.12 cm^3·g^{-1}) and high specific surface area (728 m^2·g^{-1}) (Table 1). The low-angle XRD pattern (Figure 1a) of the replica Co_3O_4 shows five well-resolved reflections, which can be indexed as (100), (110), (200), (210), and (300) reflections of

p6mm symmetry, characteristic for the two-dimensional (2-D) hexagonal structure, indicating good replication of the silica template. The mesostructure is retained very well after template removal, although the template was impregnated only once with the precursor solution. The wide-angle XRD pattern (Figure 1b) of Co_3O_4 material shows well-resolved reflections that can be assigned to the Co_3O_4 phase with spinel-type structure (PDF2 entry 42-1467), indicating well-crystallized nanomaterial.

H_2-TPR results (Figure S2) of mesoporous Co_3O_4 show three typical reduction signals. A small peak is observed around 200 °C, which can be attributed to the reduction of surface Co^{3+} species. The second one, at approximately 330 °C, is associated with the reduction of Co^{3+} ions to Co^{2+} (eq 1) with the corresponding structural change to CoO.[38−40] The third broad peak, between 370 and 570 °C, shows two features that are due to the reduction of CoO to metallic cobalt (eq 2). On the basis of these results, the reduction of mesoporous Co_3O_4 to CoO was performed at 250 °C under a 4.5 vol % H_2 atmosphere. The low-angle XRD pattern (Figure 1a) of the obtained material shows similar reflections to those observed for the original Co_3O_4 material, suggesting the well-retained mesostructure after the H_2 reduction process. The wide-angle XRD pattern (Figure 1b) of the H_2-treated material shows well-resolved reflections that can be assigned to the CoO phase with rock-salt structure (PDF2 entry 43-1004), indicating complete phase transformation from Co_3O_4 to CoO.

$$Co_3O_4 + H_2 \rightarrow 3CoO + H_2O \qquad (1)$$

$$CoO + H_2 \rightarrow Co + H_2O \qquad (2)$$
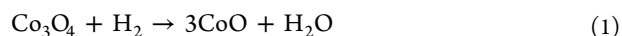
HR-SEM and TEM images of the replica Co_3O_4 are shown in Figure 2a−d and Figure S3a,b. Almost all the obtained Co_3O_4 particles have rod-like morphology, which is replicated from the SBA-15 template,[34] indicating good replication of the silica template. Each single particle is composed of ordered arrays of small nanorods/nanowires. The HR-SEM (Figure 2b) and TEM (Figure 2c) images of Co_3O_4 give a clear indication that the rod diameter is in agreement with the pore size of the silica template, further confirming that the Co_3O_4 phase was formed predominantly inside the porous silica phase. The HR-TEM (Figure 2d) image clearly reveals the crystalline nature of the mesoporous Co_3O_4. The HR-SEM (Figure 2f) and TEM (Figure 2g and Figure S3d) images of mesoporous CoO show similar particle morphology and single nanorod/nanowire width, suggesting that the phase transformation occurs in a pseudomorphic manner, without reconstruction of the whole framework. The HR-TEM (Figure 2h) image shows that the structure lattice stretches over several neighboring nanorods/ nanowires, suggesting that single-crystalline domains are bigger than the rod diameter. This may be due to the interaction between the nanorods during the structural transformation from Co_3O_4 to CoO.

The nitrogen adsorption−desorption isotherms and pore size distributions (Figure 3) of the replica Co_3O_4 and CoO materials are rather similar. They are characterized by a small capillary condensation step at relative pressures around 0.4−0.6 that is attributed to adsorption in mesopores that were generated by the removal of the silica walls. Another capillary condensation step at slightly higher relative pressures, related to larger pores, is most likely due to the partially incomplete replication of the silica template. The corresponding BET surface areas (Table 2) for Co_3O_4 and CoO are 87 and 82 m^2·
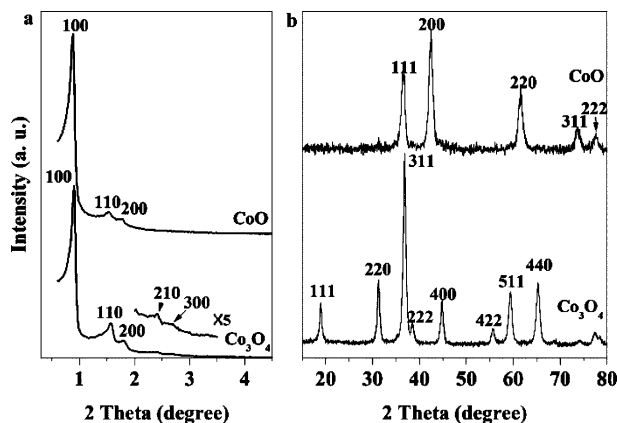

Figure 1. Low-angle (a) and wide-angle (b) XRD patterns of ordered mesoporous Co_3O_4 nanocast from SBA-15 and CoO reduced from Co_3O_4.
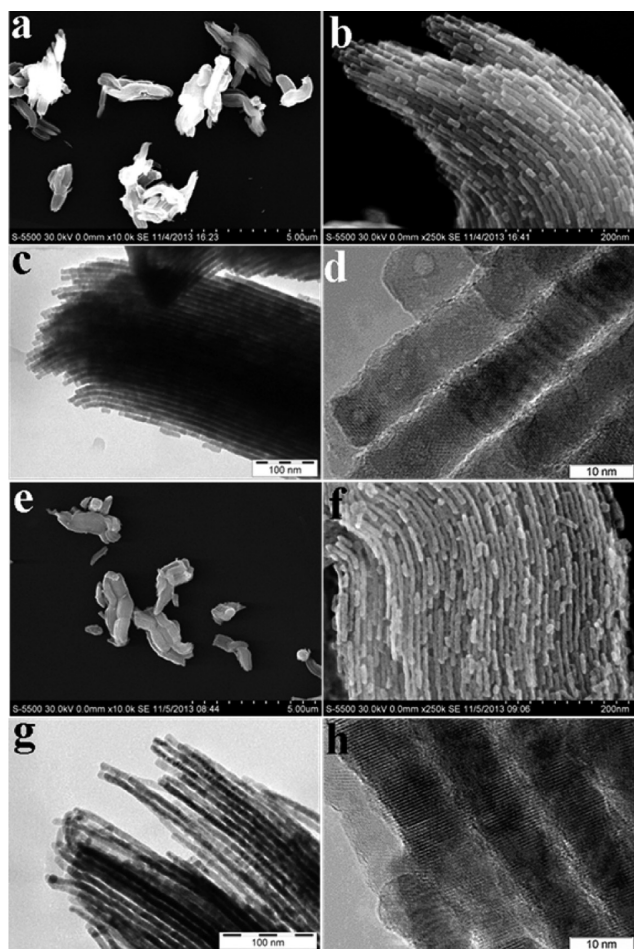
Figure 2. HR-SEM (a, b, e, and f) and TEM (c, d, g, and h) images of ordered mesoporous Co_3O_4 (a−d) and CoO (e−h) nanocast from SBA-15. CoO is reduced from mesoporous Co_3O_4 with 4.5 vol % H_2 at 250 °C for 1.5 h.

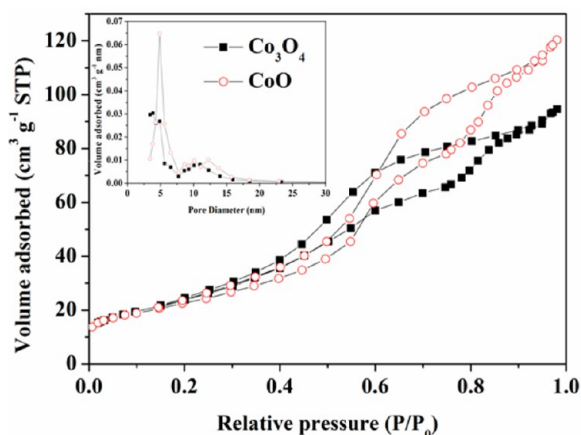**Figure 3.** Nitrogen adsorption−desorption isotherms and pore size distribution curves (inset) of mesoporous Co_3O_4 and CoO nanocast from SBA-15.

g^{-1}, respectively, suggesting only minor textural changes during the reduction process with H_2. These specific surface areas are relatively high, considering the high density of the metal oxides and the low level of microporosity.

The mesoporous CoO was tested for CO oxidation, and the results are shown in Figure 4a and summarized in Table 2. Due

to the low stability of CoO at high temperature in air, the catalyst was pretreated in He flow at 300 °C for 30 min to remove any molecules adsorbed at the surface before the catalytic test. Surprisingly, the catalytic activity of mesoporous CoO under dry gas condition at a space velocity of 80 000 mL· $h^{-1}·g_{cat}^{-1}$ (Figure 4a) shows a CO conversion of around 30% at −50 °C. With increasing temperature the CO conversion increases to more than 80% below 0 °C and slowly reaches 100% CO conversion at around 140 °C. At a temperature of −38 °C a conversion of 50% CO (T_{50}) is achieved. The wide-angle XRD pattern (Figure S4) of the used CoO catalyst shows reflections with positions almost identical to the fresh sample. The results above indicate that the mesoporous CoO material has unexpectedly high catalytic activity for CO oxidation and that its structure is quite stable during the CO oxidation process at the temperatures tested. As a comparison, mesoporous Co_3O_4 catalyst was tested for CO oxidation under the same conditions. The temperature dependence curve (Figure 4b) shows a CO conversion of about 50% at −50 °C. With increasing temperature the CO conversion increases rapidly to 100%, suggesting a higher activity than that of mesoporous CoO.

The surface composition and chemical states of the catalysts were analyzed by XPS. The evaluation of the Co 2p narrow scans allows the assignment of the oxidation state of cobalt. As reference materials for mixed $Co^{2+/3+}$ oxidation states, bulk Co_3O_4 was measured. As reference material for Co^{2+}, CoO was chosen, and as reference for pure Co^{3+}, $Co(NH_3)_6Cl_3$ was analyzed (Figure 5). Pure Co^{2+} can be distinguished from mixed Co^{2+}/Co^{3+} oxidation state by the binding energy and the intensities of the shake-up peaks of the Co 2p photopeak. Pure Co^{3+} shows only a very weak shake-up peak at 791 eV, whereas pure Co^{2+} has pronounced shake-up peaks at about 785 and 802 eV. If both oxidation states are present, instead of distinct shake-up peaks, a kind of plateau is observed. The similarity of the spectra for mesoporous Co_3O_4 indicates that the surface is similar to that of the Co_3O_4 reference material (Figure 5d), representing mixed oxidation states for cobalt. For the mesoporous CoO, two obvious shake-up peaks at about 785 and 802 eV are observed (Figure 5e). The intensive peak at 785 eV peak indicates a higher fraction of Co^{2+} species present on the surface as expected for perfect Co_3O_4.

Generally, Co^{3+} on the catalyst surface is thought to provide the active site for CO oxidation, while Co^{2+} is considered inactive.[41] Langell and co-workers[24] found that the CoO (100) single crystal surface could be oxidized to form a thin layer of Co_3O_4 when annealed in oxygen at 500 °C. However, in our case, the sample is only exposed to air at room temperature and the XPS results show that the catalyst surface is rich in Co^{2+} species. The high activity of mesoporous CoO indicates that the oxidation state of the cobalt species may not be the only reason for the catalytic activity in CO oxidation.

In order to understand the origin of the catalytic activity of mesoporous CoO for CO oxidation in more detail, a series of comparison tests was performed. The mesoporous Co_3O_4 material was normally preactivated in situ with the reaction gas (1 vol % CO, 20 vol % O_2, and 79 vol % He gas mixture) for 30 min at 300 °C. Since CoO can be easily oxidized to Co_3O_4 at low temperature in air,[42] a lower pretreatment temperature of 200 °C was used for the comparison with CoO. However, the wide-angle XRD data (Figure S5a) show that the CoO material was partially reoxidized to Co_3O_4 even at a low-temperature (200 °C) oxidative activation. The CoO content

Table 2. Physicochemical Properties and CO Oxidation Activities of Co-Based Mesoporous Catalysts with Different Compositions

sample name[a]	BET surface area ($m^2 \cdot g^{-1}$)	pore volume ($cm^3 \cdot g^{-1}$)	pore size (nm)	crystalline domain size (nm)[b]	T_{50} (°C)	T_{50} (°C) dry[c]
SBA-15	728	1.12	8.5			
Co_3O_4 (He)	87	0.15	4.9/11.0	14		<−50
Co_3O_4	87	0.15	4.9/11.0	14	111	−25
CoO (He)	82	0.19	4.9/12.2	9		−37.7
CoO	82	0.19	4.9/12.2	9	96	−9
$CuCo_2O_4$	66	0.10	4.9	10	105	8 (−4)
$CoCr_2O_4$	142	0.25	6.7	6	294	279 (285·
$CoFe_2O_4$	143	0.39	4.9	5	223	265 (177)

[a]The Co_3O_4 and CoO samples were treated with He or a 1 vol % CO, 20 vol % O_2, and 79 vol % He gas mixture before the catalytic tests; for the He-treated ones, an SV of 80 000 $mL \cdot h^{-1} \cdot g_{cat}^{-1}$ was used. For the other samples 600 000 $mL \cdot h^{-1} \cdot g_{cat}^{-1}$ was used. [b]Mean size of crystalline domains, calculated from XRD reflection broadening with the Scherrer equation (using NIST Si (640 c) to account for instrumental broadening). [c]Number in parentheses is the T_{50} with the sample weight adjusted to contain the same amount of Co species in all experiments.
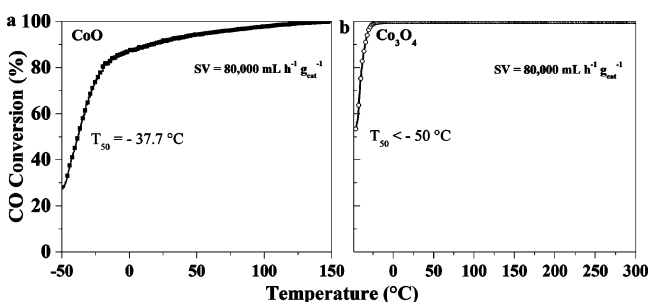

Figure 4. Temperature dependence of the activity for CO oxidation for mesoporous CoO and Co_3O_4 catalysts nanocast from SBA-15. Operation conditions: 50 mg of catalyst, 67 mL·min^{-1}; WHSV = 80 000 mL·h^{-1}·g$_{cat}^{-1}$, 1 vol % CO, 20 vol % O_2, and He balance. The catalysts were pretreated in He at 300 °C for 30 min. The feed gas was passed through a molecular sieve trap cooled to −78 °C (2-propanol/dry ice bath) before going into the reactor.

after the treatment was estimated to be around 10 wt %, which is very close to 11.6 wt % as calculated from the model illustrated in Figure S5b (assuming a rod diameter of the CoO of 6 nm and the first 2 nm of the surface being oxidized to Co_3O_4). In other words, about five layers of the CoO nanorods were oxidized to Co_3O_4 (assuming the surface is formed by (111) faces and the thickness of five layers is around 2.33 nm), which is quite similar to the results obtained in previous reports.[24] The temperature dependence of the CO conversion for CoO (Co_3O_4/CoO composite) and Co_3O_4 under different conditions is given in Figure 6 and additionally summarized in Table 2. The catalytic activity of mesoporous CoO (Co_3O_4/CoO composite) under normal gas conditions (with ∼3 ppm of H_2O) at a space velocity of 80 000 mL·h^{-1}·g$_{cat}^{-1}$ (Figure 6a) shows a "U"-shaped curve with a minimum at around 72 °C (CO conversion: 72%), which had previously been observed for Co_3O_4/SiO_2 composite materials,[23] indicating negative apparent activation energies. Adsorbed H_2O molecules on the surfaces of the catalysts had been identified as the origin of the negative apparent activation energies at intermediate temperature under normal gas conditions by *in situ* DRIFT measurements.[23] The detrimental effect of adsorbed water was fostered by DFT studies on H_2O adsorption and its effect on CO oxidation over Co_3O_4. H_2O adsorption at Co^{oct} sites via hydrogen bonding to the O^{2f} site was found to inhibit CO interaction with O^{2f} sites and then further hinders the CO_2 formation by abstracting O^{2f} atoms to a certain extent.[43,44] Under dry gas conditions (H_2O < 1 ppm), the CO conversion
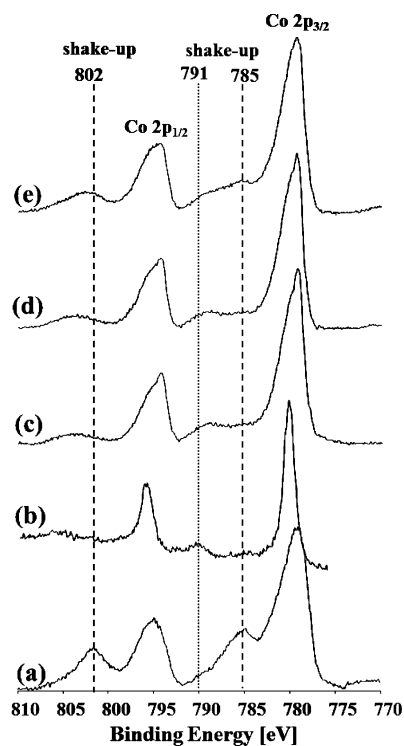

Figure 5. Co 2p XPS spectra of (a) CoO reference material, (b) Co_3O_4 reference material, (c) $Co(NH_3)_6Cl_3$ reference material, (d) mesoporous Co_3O_4 nanocast from SBA-15, and (e) mesoporous CoO reduced from mesoporous Co_3O_4 by H_2.

at around 75 °C reaches only 98%. For mesoporous Co_3O_4 under normal gas conditions at a space velocity of 80 000 mL·h^{-1}·g$_{cat}^{-1}$, a "U"-shaped curve with a minimum at around 106 °C (CO conversion: 97%) is observed (Figure 6c). However, under dry gas conditions, no region with negative apparent activation energy was observed. The CO conversions over CoO under both normal and dry gas conditions are higher than for Co_3O_4 material at very low temperature (close to −50 °C), even with the preactivation temperature being 100 °C lower than for the latter one. The T_{50} values (temperature for 50% CO conversion) of both materials are even lower than −50 °C.

In order to investigate the catalytic behavior in more detail, catalysts were evaluated at very high space velocity (600 000 mL·h^{-1}·g$_{cat}^{-1}$). The catalytic results are shown in Figure 6b,d and summarized in Table 2. The CO conversion over CoO material under normal gas conditions shows almost no activity
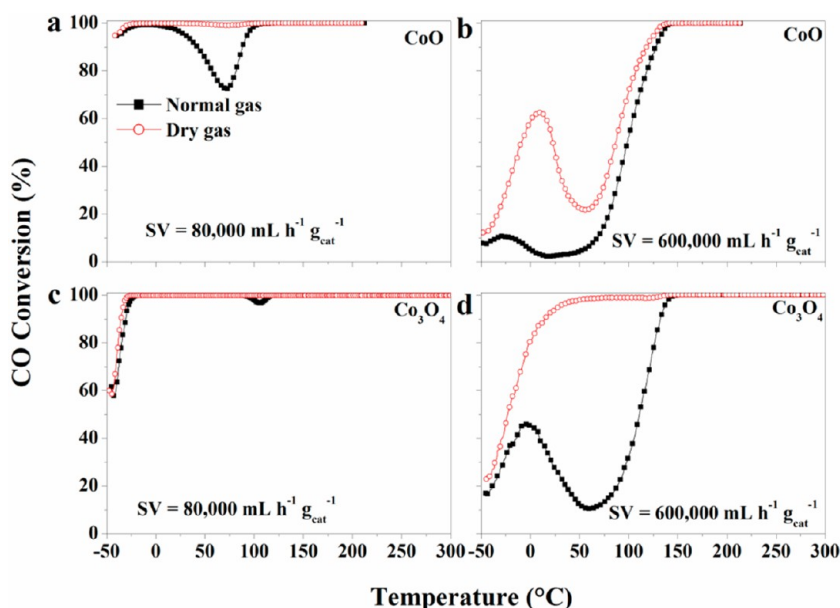
Figure 6. Temperature dependence of the activity for CO oxidation for mesoporous CoO (a, b) and Co_3O_4 (c, d) catalysts nanocast from SBA-15. (a, c) 50 mg of catalyst; reaction gas flow rate, 67 mL·min^{-1}; SV = 80 000 mL·h^{-1}·g$_{cat}$$^{-1}$. (b, d) 10 mg of catalyst; reaction gas flow rate, 100 mL·min^{-1}; SV = 600 000 mL·h^{-1}·g$_{cat}$$^{-1}$. The catalysts were pretreated in a 1 vol % CO, 20 vol % O_2, and 79 vol % He gas mixture at 200 (CoO) or 300 °C (Co_3O_4) for 30 min. For measurement under dry conditions, the feed gas was passed through a molecular sieve trap cooled to −78 °C (2-propanol/dry ice bath) before going into the reactor.
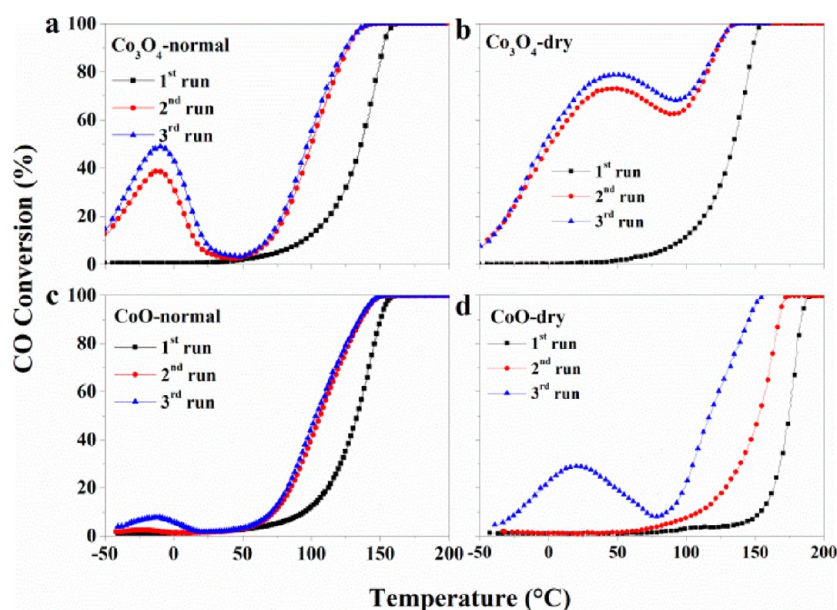

Figure 7. Temperature dependence of the activity for CO oxidation for H_2-pretreated mesoporous Co_3O_4 and CoO catalysts. (a, b) Co_3O_4. (c, d) CoO. Test conditions: 10 mg of catalyst, reaction gas flow rate, 100 mL·min^{-1}; SV = 600 000 mL·h^{-1}·g$_{cat}$$^{-1}$. The catalysts were treated in H_2 at 200 °C for 30 min before tests. For measurement under dry conditions, the feed gas was passed through a molecular sieve trap cooled to −78 °C (2-propanol/dry ice bath) before going into the reactor.

at temperatures below 50 °C, whereas under dry gas conditions, an obvious "U"-shaped curve can be observed with a turning point at 55 °C and 22% CO conversion. For Co_3O_4 under normal gas conditions, the CO conversion at temperatures below 150 °C drops significantly, as expected. The bottom of the "U"-shaped curve is around 62 °C with a CO conversion of only 12%. Even under dry gas conditions, the CO conversion does not reach 100% at 120 °C. The light-off curves for the first and second run are almost identical for all the samples (Figure S6), indicating the reproducibility of this effect. Conversion

curves were also found to be reproducible to within a few percent conversions at identical temperature for separately synthesized batches of catalysts.

For comparison, a commercial CoO material with a particle size of ~325 mesh (Aldrich) was measured under the same conditions for CO oxidation. The wide-angle XRD pattern (Figure S7) of the commercial CoO catalyst shows very sharp reflections, indicating large crystallites. The reflections can be assigned to the rock-salt-type structure of CoO. A small reflection around 44.2° can be assigned to metallic cobalt. The

BET surface area calculated from the nitrogen sorption isotherm is 6 $m^2 \cdot g^{-1}$, which is much lower than the surface area of the mesoporous CoO catalyst. The light-off CO conversion curves are shown in Figure S8. A space velocity of 80 000 $mL \cdot h^{-1} \cdot g_{cat}^{-1}$ was used. The curves obtained under both normal and dry gas conditions are "U"-shaped, similar to the mesoporous CoO material at a high space velocity (600 000 $mL \cdot h^{-1} \cdot g_{cat}^{-1}$), with slightly higher activity for the mesoporous material. Considering the about 8-fold higher space velocity for the mesoporous CoO and the about 14 times higher surface area, this suggests that the catalytic properties for CO oxidation are rather similar for different types of CoO materials.

In order to further explore the nature of the active site of the mesoporous CoO materials, samples were pretreated *in situ* with H_2 to reduce potential Co^{3+} surface species. For comparison, Co_3O_4 was also treated under the same conditions. The results are shown in Figure 7. For the first runs of the light-off tests for CO oxidation over mesoporous Co_3O_4 under normal as well as under dry gas conditions, the low temperature activity disappeared, indicating that the Co^{3+} surface species play an important role in the catalytic CO oxidation (Figure 7a,b). However, the low-temperature activity was restored in the second run for both conditions and is also reproducible for the third run. This suggests that the Co^{3+} surface species in Co_3O_4 can be easily restored below 200 °C. For mesoporous CoO, the low-temperature activity also disappears after the H_2 treatment for both conditions (Figure 7c,d). Full CO conversion in the first run is archived only at 190 °C under dry gas conditions (Figure 7d). The temperature is much higher than the temperature of 155 °C observed for Co_3O_4. Even in the second run, the low temperature activity of CoO could not be restored, but the conversion curve shifts to lower temperature by about 20 °C. The low-temperature activity is restored only in the third run. These results suggest that also for the CoO catalyst the Co^{3+} surface species play a crucial role for CO oxidation and that these species can be formed during the low-temperature (200 °C) treatment in the reaction gas.

The catalytic activities under O_2-deficient conditions were also investigated by using a mixed gas with 2.140 vol % CO and 0.876 vol % O_2 balanced with He. The activities of the catalysts in the O_2-deficient atmosphere are significantly lower than those under O_2-rich conditions (Figures S9 and 6). For Co_3O_4, the CO conversion is very similar to that of CoO; this is due to (partial) reduction of Co_3O_4 to CoO at 300 °C during the pretreatment step. While pretreating the catalysts with pure He, the catalytic activities are similar to those under O_2-rich conditions (Figure S10).

It is known that the adsorption and activation of molecular oxygen are crucial for supported gold catalyst[41,45−48] and Co-based catalysts[23,49] for CO oxidation. The formation of adsorbed reactive oxygen species, such as superoxide ions (O_2^-), can be correlated to the presence of surface oxygen vacancies on the metal oxide support[46] or at the metal−support interfaces.[45−47] Different kinds of superoxide species have been reported to exist on the surface of CoO−MgO solid solution[49] and Co_3O_4/SiO_2 composite materials,[23] and it was thus hypothesized that such superoxide species may play an important role in CO oxidation and also over the mesoporous materials investigated here at low temperatures. Therefore, CO titration experiments in the absence of oxygen (1 vol % CO in N_2) were performed. This allows assessing the extent of the supply of oxygen stored on the catalyst. Figure 8 shows the transient response of the CO_2 and CO evolution over
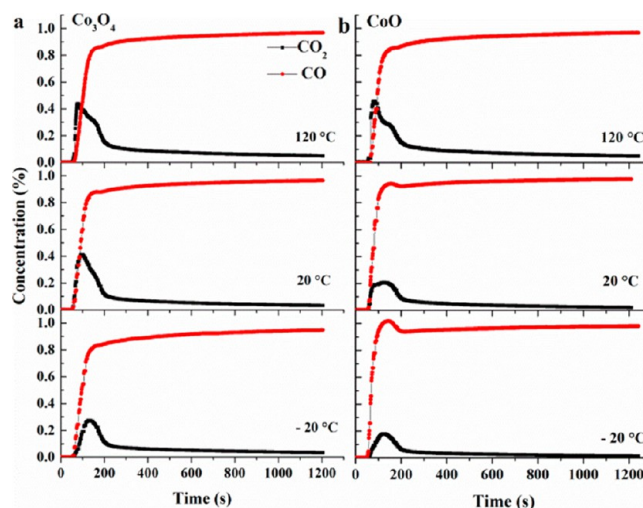

Figure 8. CO_2 response in the CO titration experiments of the pretreated (1 vol % CO, 20 vol % O_2, and 79 vol % He gas mixture) mesoporous Co_3O_4 (a) and CoO (b) catalysts at temperatures of −20, 20, and 120 °C. All the above experiments were carried out under normal conditions. 50 mg of catalyst, reaction gas, 1 vol % CO in N_2; flow rate = 67 $mL \cdot min^{-1}$.

pretreated mesoporous Co_3O_4 and CoO at different temperatures. For mesoporous Co_3O_4, the ability to provide reactive oxygen is rather high at low temperature (−20 °C). High CO_2 evolution with a maximum (CO_2 concentration 0.27%) at 125 s after exposure to CO was observed. The initial sharp CO_2 response is indicative of a fast reaction, proceeding via rapid adsorption of CO followed by the reaction of CO with the reactive oxygen on the catalyst surface. It is noticed that, even after 1000 s, substantial amounts of CO_2 were still produced (CO_2 concentration 0.04%). At 20 °C, a CO_2 response maximum was observed after 96 s with an even higher CO_2 concentration (0.41%) than that observed at −20 °C. The CO_2 evolution decreased gradually to the same level observed at −20 °C after 1000 s. At 120 °C, the CO_2 concentration peaked after 76 s (CO_2 concentration 0.44%). For mesoporous CoO catalyst, CO_2 evolution with a maximum (CO_2 concentration 0.18%) at 119 s after exposure to CO was observed. At 20 °C, a CO_2 response maximum was observed after 124 s with a maximum of 0.21%, whereas at 120 °C, a CO_2 response maximum was observed after 81 s with a maximum of 0.46%. From the above results, it can be seen that the ability of the mesoporous CoO catalyst to supply reactive oxygen is at the same level as that of the mesoporous Co_3O_4 one, except at 20 °C. However, the response time for mesoporous CoO is slightly slower than for Co_3O_4 at all temperature points investigated, suggesting a slower CO adsorption rate and/or CO reaction rate with the reactive surface oxygen species.

The integral under the curves reported in Figure 8 allows calculation of the total amount of active oxygen on the surface of the catalysts. In order to estimate whether bulk oxygen contributes to the CO oxidation in the titration experiments, the maximum amount of oxygen that could be present just on the surface was calculated. This was done under the assumption that the surface is composed of only the close-packed (111) plane of Co_3O_4 or CoO. The calculation method was reported in our previous work.[23] For both Co_3O_4 and CoO under different temperatures, the amount of the consumed oxygen is lower than this maximum amount (Table 3). However,

Table 3. Amount of Oxygen Consumed from Mesoporous Spinel Catalysts in CO Titration Experiments

| sample name	maximum surface O^{2-} (μmol)[a]	temperature (°C)	O consumption (μmol)	O consumption per unit area ($\mu mol/m^2$)
Co_3O_4	114.7	−20	42.7	9.82
		20	52.6	12.09
		120	66.8	15.36
CoO	86.2	−20	24.2	5.90
		20	35.2	8.59
		120	65.5	15.98
$CuCo_2O_4$	58.1	−20	20.6	6.24
		20	36.0	10.91
		120	108.1	32.76
$CoCr_2O_4$	187.2	−20	1.0	0.14
		20	2.3	0.32
		120	8.7	1.23
$CoFe_2O_4$	133.5	−20	11.4	1.59
		20	17.9	2.50
		120	49.1	6.87

[a]Maximum surface oxygen (O^{2-}) capacities of the catalysts are calculated with the assumption that the surface of the catalysts is composed only of (111) surface. The surface areas of the spinel catalysts used are listed in Table 2. The catalyst amount for CO titration is 50 mg.

considering that the surface of the catalysts most probably does not consist only of the (111) plane, but also other faces with lower oxygen density, or could contain residual amorphous silica (bulk residual silica around 1 wt %), the true amount of surface oxygen is probably lower than the ideally calculated values. The O consumption normalized to unit surface area (Table 3) shows that mesoporous Co_3O_4 and CoO have very similar numbers at −20 and 120 °C. Co_3O_4 contains more reactive oxygen than CoO per unit surface as well as per weight at low temperatures, corresponding well to the CO oxidation activities shown in Figure 6b and d.

In situ DRIFT spectroscopy was also used to detect CO adsorbed on the surfaces of CoO and Co_3O_4 catalysts at room temperature. The spectra under CO adsorption conditions (Figure S11) for both CoO and Co_3O_4 catalysts reveal the characteristic gas-phase bands of CO at 2117 and 2171 cm^{-1}, but no strongly adsorbed CO-$Co^{\delta+}$ was detected. No obvious differences in CO adsorption over CoO and Co_3O_4 were observed. It is noticed that in the range 1300−1700 cm^{-1}, which corresponds to various vibrations of carbonates, differences for CoO and Co_3O_4 indeed exist, especially in the CO adsorption process. However, it is rather difficult to assign these bands precisely, as reflected by oppositional reports in the literature.

Mesoporous CoO also could be synthesized via reduction with CO. The respective data are shown in the Supporting Information (Figures S12−14). The structure of the material and its CO oxidation activities are similar to that prepared via reduction with H_2.

The experimental results presented above show that mesoporous CoO has unexpected activity in CO oxidation. The activity may be related to oxidation of surface Co^{2+} species in octahedral coordination, which results in rather similar sites to the Co^{3+} in the cobalt oxide spinel. Structurally, at 300 K CoO has a rock-salt structure with a single Co^{2+} site, octahedrally coordinated by lattice oxygen in $Fm\bar{3}m$ symmetry (Figure 9b).[24,25] Co_3O_4 has a spinel structure with $Fd\bar{3}m$
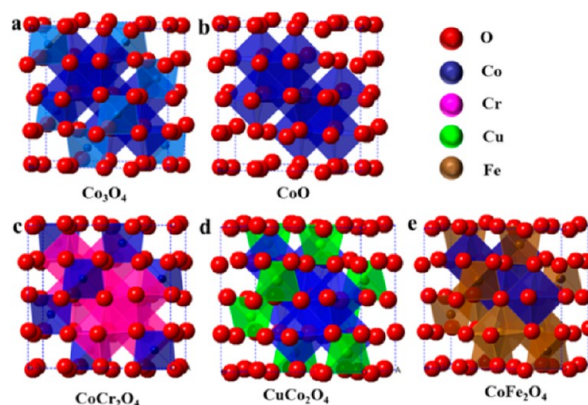
Figure 9. Three-dimensional structures of metal oxides: (a) Co_3O_4, (b) CoO, (c) $CoCr_2O_4$, (d) $CuCo_2O_4$, and (e) $CoFe_2O_4$.

symmetry (Figure 9a). The Co^{3+} cation in the spinel structure is octahedrally coordinated, while Co^{2+} is tetrahedrally coordinated. The two structures are strongly related through their oxygen sublattices. Both spinel and rock-salt lattice oxygen are face centered cubic (*fcc*), with the $O^{2-}-O^{2-}$ closest packing distance in the rock-salt structure ∼5% larger than in the spinel structure.

In rock-salt all octahedral sites are filled, but only half are filled in the spinel structure. The tetrahedral sites, which are completely unoccupied in the rock-salt structure, are partially filled to one-eighth occupancy in the spinel structure. The Co^{2+} species in CoO occupy the position that corresponds to the Co^{3+} species in Co_3O_4. The octahedrally coordinated sites in CoO are more open than the tetrahedrally coordinated sites in Co_3O_4, which allows easy oxidation of the Co^{2+} species to Co^{3+}, resulting in high activity. If all surface Co^{2+} species in the CoO were oxidized to Co^{3+}, their surface density would actually be higher than in the spinel structure, which could explain the even higher catalytic activity at low temperature compared to the parent Co_3O_4 material (Figure 6a and c). In addition, the surface oxidized CoO may contain a few layers of cobalt oxides with a somewhat different structure compared to normal Co_3O_4 spinel,[24] which could lead to the higher catalytic activity of the composite material compared to the normal mesoporous Co_3O_4.

3.2. Other Co-Based Spinel Mesoporous Catalysts. The structure of CoO is related to the spinel structure. Several spinels with different Co species substituted by non/low-active metal ions ($CuCo_2O_4$, $CoCr_2O_4$, and $CoFe_2O_4$) were synthesized in order to investigate whether only the octahedrally coordinated Co^{2+} species can be oxidized to Co^{3+} and thus result in an active catalyst. The position of each cation is summarized in Table 1. In $CuCo_2O_4$, the tetrahedrally coordinated Co^{2+} is substituted by Cu^{2+} (Figure 9d). In $CoCr_2O_4$, the octahedrally coordinated Co^{3+} is substituted by Cr^{3+} (Figure 9c). $CoFe_2O_4$ is an inverse spinel structure, in which half of Fe^{3+} is tetrahedrally coordinated and the other half of Fe^{3+} is located together with the Co^{2+} ions in the octahedrally coordinated position (Figure 9e).

All spinels were synthesized using the same nanocasting route, starting with SBA-15 as used for the synthesis of mesoporous Co_3O_4. Metal nitrates with the required molar ratios were used as precursors. The low-angle XRD pattern (Figure 10A(a)) of the $CuCo_2O_4$ shows three well-resolved reflections, indicating good replication of the silica template. The peak positions are similar to those of mesoporous Co_3O_4,
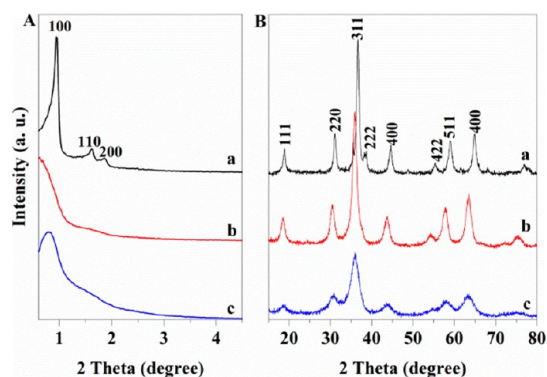
Figure 10. Low-angle (A) and wide-angle (B) XRD patterns of mesoporous cobalt-based spinels nanocast from SBA-15: (a) $CuCo_2O_4$, (b) $CoCr_2O_4$, and (c) $CoFe_2O_4$.

indicating that both have similar structures. In contrast, for $CoCr_2O_4$, only weak reflections are observed, indicating lower structural ordering. However, the wide-angle XRD patterns (Figure 10B) of all the replica materials show broader reflections than normally observed for the spinel phases, indicating the formation of nanomaterials.

TEM images of the spinel replicas are shown in Figure 11. $CuCo_2O_4$ exhibits well-ordered nanorod/nanowire arrays with rod-like particle morphology. This also supports the notion that the replication of the SBA-15 silica template worked well. For $CoFe_2O_4$, only little order is observed in the mesostructured range, as reflected by rather broad low-angle XRD reflections. For $CoCr_2O_4$, only small nanorods with similar diameters to all the other mesoporous materials can be observed in TEM images, again in agreement with the results of the low-angle

XRD analyses. Nitrogen adsorption−desorption isotherms (Figure S15) measured for the Co-based spinels show the shape typical for mesoporous replicated metal oxides. Physicochemical properties of the samples are summarized in Table 2. The specific surface areas differ more strongly due to the stronger variety of structural ordering and densities among these samples. However, all samples were synthesized using the same method and the same template. The sizes of the individual particles/rods for all samples are controlled by the pore size of the silica template. Thus, the domain sizes of the different catalysts still remain comparable (Table 2), and thus their catalytic properties should be comparable as well to some extent, even if the similarities are less pronounced than for the Co_3O_4/CoO system.

The catalytic activities of the spinel catalysts for CO oxidation were tested in the same reactor as used for the experiments discussed earlier, using a 1 vol % CO, 20 vol % O_2, and 79 vol % He gas mixture. The temperature dependence of the CO conversions at a space velocity of 600 000 mL·h^{-1}·g$_{cat}^{-1}$ is shown in Figure 12a and b. Mesoporous $CuCo_2O_4$, containing only octahedrally coordinated Co^{3+} species, shows catalytic activity at low temperatures, under both normal and dry gas conditions. The T_{50} temperature under dry gas conditions was determined to be 8 °C. As for the Co_3O_4 and the CoO, a "U"-shaped curve is observed with a minimum around 75 °C, indicating that the negative apparent activation energy in CO oxidation is common for Co-based metal oxides. In contrast, mesoporous $CoCr_2O_4$ and $CoFe_2O_4$ show very low catalytic activities under both normal and dry gas conditions. The T_{50} temperatures determined under dry gas conditions are 294 and 223 °C, respectively. In order to normalize the samples for cobalt content, measurements for equal amounts of Co

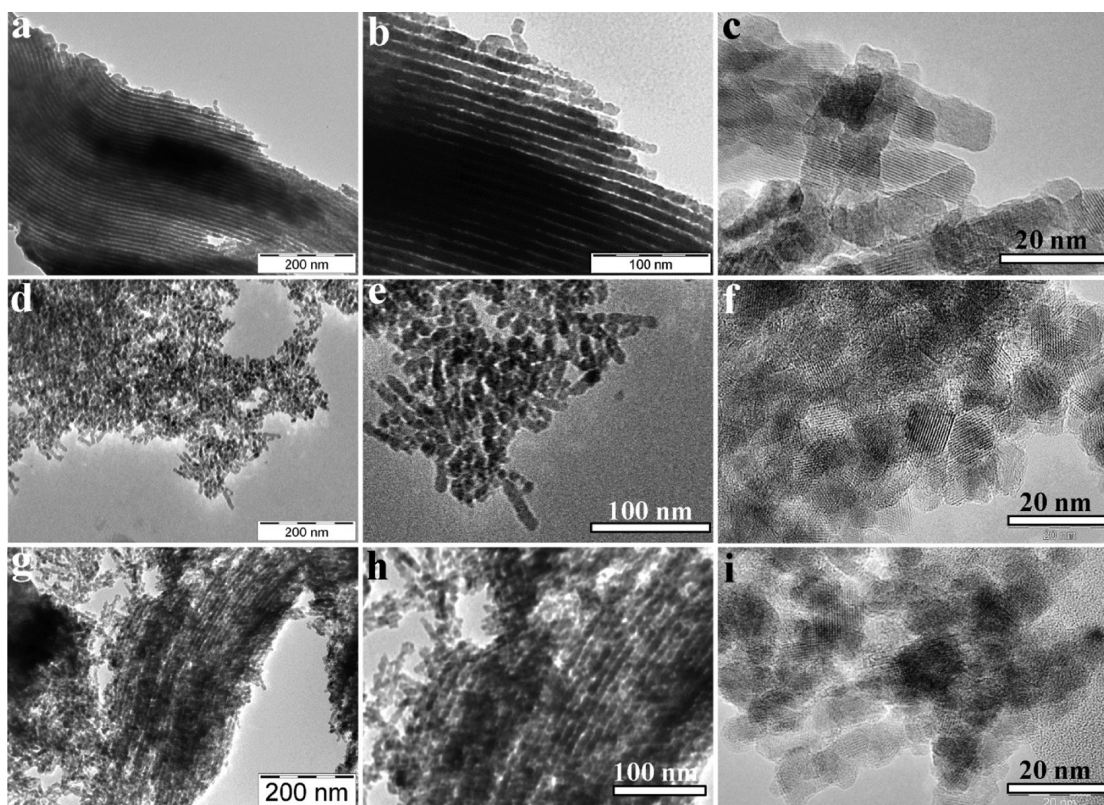**Figure 11.** TEM images of cobalt-based spinels: (a−c) $CuCo_2O_4$, (d−f) $CoCr_2O_4$, and (g−i) $CoFe_2O_4$.
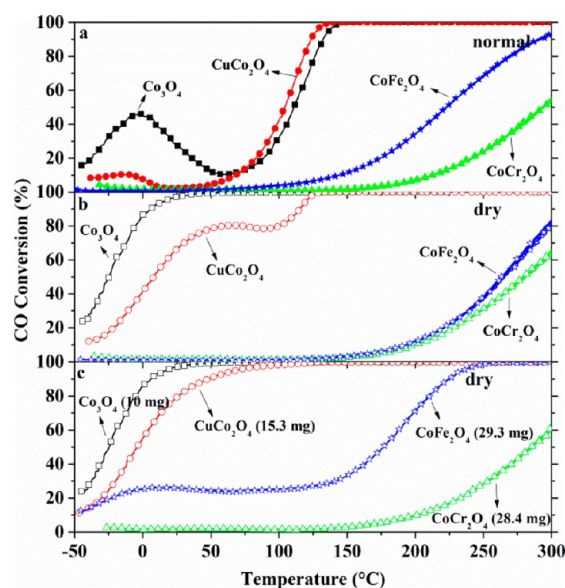
Figure 12. Temperature dependence of the activity for CO oxidation for mesoporous spinels (Co_3O_4, $CuCo_2O_4$, $CoCr_2O_4$, and $CoFe_2O_4$) nanocast from SBA-15. (a, b) 10 mg of catalyst; reaction gas flow rate = 100 mL·min^{-1}; SV = 600 000 mL·h^{-1}·g$_{cat}^{-1}$. (c) Catalyst: 10 mg of Co_3O_4, 15.3 mg of $CuCo_2O_4$, 28.4 mg of $CoCr_2O_4$, and 29.3 mg of $CoFe_2O_4$; reaction gas flow rate = 100 mL·min^{-1}. For measurements under dry conditions, the feed gas was passed through a molecular sieve trap cooled to −78 °C (2-propanol/dry ice bath) before going into the reactor.

species by adjusting the catalyst weight were carried out under dry gas conditions. A 15.3 mg amount of $CuCo_2O_4$, 28.4 mg of $CoCr_2O_4$, and 29.3 mg of $CoFe_2O_4$ were used for comparison with 10 mg of Co_3O_4. The results are shown in Figure 12c. The activity of mesoporous $CuCo_2O_4$ (T_{50} = −4 °C) increases and comes close to that of Co_3O_4 (T_{50} = −25 °C). The slightly lower activity may be due to the lower specific surface area of $CuCo_2O_4$. The T_{50} of $CoFe_2O_4$ containing octahedrally coordinated Co^{2+} decreases from 265 °C to 177 °C, while that of $CoCr_2O_4$ stays almost unchanged (from 279 °C to 285 °C). These results suggest that the octahedrally coordinated Co^{3+} species play an important role in the catalytic activity for CO oxidation, while the tetrahedrally coordinated Co^{2+} has almost no activity and can also not be easily oxidized, as compared to the octahedrally coordinated Co^{2+} species in CoO. $CoFe_2O_4$ with octahedrally coordinated Co^{2+} also shows some activity, which could be related to easy oxidation of the Co^{2+} on such sites.[50,51]

XPS characterization was performed to investigate the surface composition and chemical state of the surface atoms of the mesoporous spinel catalysts. The results are shown in Figure S16. The Co 2p XPS spectrum of mesoporous $CuCo_2O_4$ shows peaks characteristic for a mixture of Co^{2+} and Co^{3+} oxidation states. The surface seems to consist of Co^{2+} and Co^{3+} comparable to reference Co_3O_4. The Co 2p XPS spectrum of mesoporous $CoCr_2O_4$ shows a strong shake-up peak at 785 eV, which is typical for Co^{2+}. For mesoporous $CoFe_2O_4$, two intensive shake-up peaks at about 785 and 791 eV are observed, indicating both Co^{2+} and Co^{3+} on the surface. Nevertheless, the intensity of the shake-up peak at 785 eV is slightly higher than expected for stoichiometric Co^{2+}–Co^{3+} distribution, indicating that this sample contains a slightly higher concentration of Co^{2+} species on the surface compared to the reference Co_3O_4. The

results above also indicate that the octahedrally coordinated Co^{2+} in $CoFe_2O_4$ is more easily oxidized than tetrahedrally coordinated Co^{2+} in $CoCr_2O_4$. The stoichiometric ratios of Co/Cu, Co/Cr, and Co/Fe on the surfaces were calculated by XPS to be 34:66, 36:64, and 38:62, respectively, which is more or less identical to the bulk compositions.

The oxygen storage capacity is related to the metal–oxygen bond energy.[52] Metal oxides, such as Co_3O_4, have lower metal–oxygen bond energy, leading to the abstraction of oxygen from the surface of the metal oxide to form surface oxygen vacancies. This finally enhances the adsorption of oxygen for CO oxidation. In order to compare the oxygen stored on the ion-substituted mesoporous spinel catalysts with that of Co_3O_4, CO titration experiments in the absence of oxygen (1 vol % CO in N_2) were also performed for these samples. Figure S17 shows the transient response of the CO_2 and CO evolution over pretreated mesoporous $CuCo_2O_4$, $CoCr_2O_4$, and $CoFe_2O_4$ at different temperatures. The corresponding oxygen consumptions are also summarized in Table 3. From the results, it can be concluded that the high activity of $CuCo_2O_4$ at low temperatures is related to a high oxygen storage capacity. In comparison, $CoCr_2O_4$ has almost no oxygen storage capacity at temperatures below 120 °C due to its higher Cr–O bonding energy. For $CoFe_2O_4$, the oxidizable Co^{2+} species is located on the octahedrally coordinated position, which is more accessible than the tetrahedrally coordinated one. This leads to a small amount of oxygen stored.

For the different Co-substituted spinels, the catalytic activities for CO oxidation are related not only to their cobalt valence state but also to the position of the cobalt species in the crystal structure. $CuCo_2O_4$ with only octahedrally coordinated Co^{3+} species can have a comparable activity to Co_3O_4. $CoCr_2O_4$ with only tetrahedrally coordinated Co^{2+} is almost completely inactive. No surface Co^{3+} can be detected by the XPS measurements. Co^{2+} in $CoFe_2O_4$ is octahedrally coordinated, which is similar to the coordination of Co in CoO. This site can be oxidized to some extent and results in moderate activity of $CoFe_2O_4$.

While accessibility is a kinetic argument for the preferred oxidation of Co^{2+} in octahedral sites, oxidation of octahedrally coordinated Co^{2+} should also be easier from an energetic point of view. In a simple ligand field theory picture, octahedral Co^{3+} ($t_{2g}^6 e_g^0$) is energetically substantially favored over Co^{2+} ($t_{2g}^6 e_g^1$ or $t_{2g}^5 e_g^2$) in a moderate ligand field, such as provided by an oxide environment, while for tetrahedral coordination the ligand field stabilization of Co^{3+} ($e_g^3 t_{2g}^3$) over Co^{2+} ($e_g^4 t_{2g}^3$) is relatively small. There is thus a higher driving force for oxidation of Co^{2+} in octahedral environment. Which of the two factors is more important or if both contribute cannot be decided based on the available data.

4. CONCLUSION

In summary, we have synthesized a series of mesoscopically ordered and crystalline spinel-type metal oxides (Co_3O_4, $CuCo_2O_4$, $CoCr_2O_4$, and $CoFe_2O_4$). All materials were obtained by nanocasting from the same silica template. This results in compounds with relatively similar nanostructures—albeit with different degrees of mesostructural order—and textural parameters. Furthermore, these materials are structurally related on the atomic scale, but contain cobalt species in different coordination environments and oxidation states. Thus, these materials are highly suitable to study the active sites for CO oxidation over Co-based catalysts. Highly ordered

mesoporous CoO was prepared by a low-temperature H_2 reduction method. This CoO material shows unexpectedly high activity in CO oxidation, which is attributed to surface oxidation of the octahedrally coordinated Co^{2+} species in the relatively open CoO rock-salt structure. A series of metal ion substituted spinels ($CuCo_2O_4$, $CoCr_2O_4$, and $CoFe_2O_4$) was synthesized to further investigate the origin of high activity in CO oxidation. The experimental data reveal that the valence state of the cobalt species is important for the catalytic activity. The coordination environment also plays a crucial role in that it controls the oxidizability of the Co^{2+} species. The octahedrally coordinated Co^{2+} is located in a more open framework site than the tetrahedrally coordinated Co^{2+}, and the crystal-field stabilization energies (CFSE) of Co^{2+} is much lower than that of Co^{3+}, which makes the former more accessible to oxygen and more easily oxidized to Co^{3+}. This is proposed as the origin of the high activity of CoO material, which is thus a true surface effect. In spite of the reduced bulk material, the surface layer provides the oxidized Co^{3+} species that are crucial for activity.

■ ASSOCIATED CONTENT

ⓢ Supporting Information

The Supporting Information is available free of charge on the ACS Publications website at DOI: 10.1021/jacs.5b06336.

> Additional results of XRD, TEM, XPS, TPR, nitrogen sorption, DRIFT, and CO oxidation results (PDF)

■ AUTHOR INFORMATION

Corresponding Authors

*schueth@mpi-muelheim.mpg.de
*jiacj@sdu.edu.cn

Notes

The authors declare no competing financial interest.

■ ACKNOWLEDGMENTS

■ REFERENCES

(1) Kresge, C. T.; Leonowicz, M. E.; Roth, W. J.; Vartuli, J. C.; Beck, J. S. *Nature* **1992**, *359*, 710.

(2) Zhao, D. Y.; Feng, J. L.; Huo, Q. S.; Melosh, N.; Fredrickson, G. H.; Chmelka, B. F.; Stucky, G. D. *Science* **1998**, *279*, 548.

(3) Yang, P. D.; Zhao, D. Y.; Margolese, D. I.; Chmelka, B. F.; Stucky, G. D. *Nature* **1998**, *396*, 152.

(4) Ryoo, R.; Joo, S. H.; Jun, S. *J. Phys. Chem. B* **1999**, *103*, 7743.

(5) Soler-illia, G. J. D.; Sanchez, C.; Lebeau, B.; Patarin, J. *Chem. Rev.* **2002**, *102*, 4093.

(6) Meng, Y.; Gu, D.; Zhang, F. Q.; Shi, Y. F.; Yang, H. F.; Li, Z.; Yu, C. Z.; Tu, B.; Zhao, D. Y. *Angew. Chem., Int. Ed.* **2005**, *44*, 7053.

(7) Wan, Y.; Zhao, D. Y. *Chem. Rev.* **2007**, *107*, 2821.

(8) Ren, Y.; Ma, Z.; Bruce, P. G. *Chem. Soc. Rev.* **2012**, *41*, 4909.

(9) Gu, D.; Schüth, F. *Chem. Soc. Rev.* **2014**, *43*, 313.

(10) Gu, D.; Li, W.; Wang, F.; Bongard, H.; Spliethoff, B.; Schmidt, W.; Weidenthaler, C.; Xia, Y. Y.; Zhao, D. Y.; Schüth, F. *Angew. Chem., Int. Ed.* **2015**, *54*, 7060.

(11) Ren, Y.; Ma, Z.; Qian, L. P.; Dai, S.; He, H. Y.; Bruce, P. G. *Catal. Lett.* **2009**, *131*, 146.

(12) An, K.; Alayoglu, S.; Musselwhite, N.; Plamthottam, S.; Melaet, G.; Lindeman, A. E.; Somorjai, G. A. *J. Am. Chem. Soc.* **2013**, *135*, 16689.

(13) Song, H.; Rioux, R. M.; Hoefelmeyer, J. D.; Komor, R.; Niesz, K.; Grass, M.; Yang, P. D.; Somorjai, G. A. *J. Am. Chem. Soc.* **2006**, *128*, 3027.

(14) Joo, S. H.; Park, J. Y.; Tsung, C.-K.; Yamada, Y.; Yang, P. D.; Somorjai, G. A. *Nat. Mater.* **2009**, *8*, 126.

(15) Park, E. D.; Lee, D.; Lee, H. C. *Catal. Today* **2009**, *139*, 280.

(16) Landon, P.; Ferguson, J.; Solsona, B. E.; Garcia, T.; Carley, A. F.; Herzing, A. A.; Kiely, C. J.; Golunski, S. E.; Hutchings, G. J. *Chem. Commun.* **2005**, 3385.

(17) Shelef, M.; McCabe, R. W. *Catal. Today* **2000**, *62*, 35.

(18) Adams, K. M.; Graham, G. W. *Appl. Catal., B* **2008**, *80*, 343.

(19) Haruta, M.; Tsubota, S.; Kobayashi, T.; Kageyama, H.; Genet, M. J.; Delmon, B. *J. Catal.* **1993**, *144*, 175.

(20) Yamaura, H.; Moriya, K.; Miura, N.; Yamazoe, N. *Sens. Actuators, B* **2000**, *65*, 39.

(21) Xie, X. W.; Li, Y.; Liu, Z. Q.; Haruta, M.; Shen, W. J. *Nature* **2009**, *458*, 746.

(22) Antonelli, D. M.; Ying, J. Y. *Angew. Chem., Int. Ed. Engl.* **1995**, *34*, 2014.

(23) Jia, C.-J.; Schwickardi, M.; Weidenthaler, C.; Schmidt, W.; Korhonen, S.; Weckhuysen, B. M.; Schüth, F. *J. Am. Chem. Soc.* **2011**, *133*, 11279.

(24) Greenwald, S. *Acta Crystallogr.* **1953**, *6*, 396.

(25) Petitto, S. C.; Marsh, E. M.; Carson, G. A.; Langell, M. A. *J. Mol. Catal. A: Chem.* **2008**, *281*, 49.

(26) Jauch, W.; Reehuis, M.; Bleif, H. J.; Kubanek, F.; Pattison, R. *Phys. Rev. B: Condens. Matter Mater. Phys.* **2001**, *64*, 0521002/1.

(27) Lu, A.-H.; Schüth, F. *Adv. Mater.* **2006**, *18*, 1793.

(28) Gu, D.; Jia, C.-J.; Bongard, H.; Spliethoff, B.; Weidenthaler, C.; Schmidt, W.; Schüth, F. *Appl. Catal., B* **2014**, *152−153*, 11.

(29) Ghosh, M.; Sampathkumaran, E. V.; Rao, C. N. R. *Chem. Mater.* **2005**, *17*, 2348.

(30) An, K.; Lee, N.; Park, J.; Kim, S. C.; Hwang, Y.; Park, J.-G.; Kim, J.-Y.; Park, J.-H.; Han, M. J.; Yu, J.; Hyeon, T. *J. Am. Chem. Soc.* **2006**, *128*, 9753.

(31) Salabas, E. L.; Rumplecker, A.; Kleitz, F.; Radu, F.; Schüth, F. *Nano Lett.* **2006**, *6*, 2977.

(32) Tüysüz, H.; Comotti, M.; Schüth, F. *Chem. Commun.* **2008**, 4022.

(33) Tüysüz, H.; Liu, Y.; Weidenthaler, C.; Schüth, F. *J. Am. Chem. Soc.* **2008**, *130*, 14108.

(34) Zhao, D. Y.; Huo, Q. S.; Feng, J. L.; Chmelka, B. F.; Stucky, G. D. *J. Am. Chem. Soc.* **1998**, *120*, 6024.

(35) Tian, B. Z.; Liu, X. Y.; Yang, H. F.; Xie, S. H.; Yu, C. Z.; Tu, B.; Zhao, D. Y. *Adv. Mater.* **2003**, *15*, 1370.

(36) Galarneau, A.; Cambon, N.; Di Renzo, F.; Ryoo, R.; Choi, M.; Fajula, F. *New J. Chem.* **2003**, *27*, 73.

(37) Fulvio, P. F.; Pikus, S.; Jaroniec, M. *J. Mater. Chem.* **2005**, *15*, 5049.

(38) Arnoldy, P.; Moulijn, J. A. *J. Catal.* **1985**, *93*, 38.

(39) Sexton, B. A.; Hughes, A. E.; Turney, T. W. *J. Catal.* **1986**, *97*, 390.

(40) Ren, Y.; Bruce, P. G.; Ma, Z. *J. Mater. Chem.* **2011**, *21*, 9312.

(41) Jansson, J.; Palmqvist, A. E. C.; Fridell, E.; Skoglundh, M.; Osterlund, L.; Thormahlen, P.; Langer, V. *J. Catal.* **2002**, *211*, 387.

(42) Xu, X. L.; Li, J. Q. *Surf. Sci.* **2011**, *605*, 1962.

(43) Wang, H. F.; Kavanagh, R.; Guo, Y. L.; Guo, Y.; Lu, G. Z.; Hu, P. *Angew. Chem., Int. Ed.* **2012**, *51*, 6657.

(44) Tang, C.-W.; Wang, C.-B.; Chien, S.-H. *Thermochim. Acta* **2008**, *473*, 68.

(45) Haruta, M. *CATTECH* **2002**, *6*, 102.

(46) Guzman, J.; Carrettin, S.; Corma, A. *J. Am. Chem. Soc.* **2005**, *127*, 3286.

(47) Guzman, J.; Carrettin, S.; Fierro-Gonzalez, J. C.; Hao, Y. L.; Gates, B. C.; Corma, A. *Angew. Chem., Int. Ed.* **2005**, *44*, 4778.

(48) van Bokhoven, J. A.; Louis, C.; Miller, J. T.; Tromp, M.; Safonova, O. V.; Glatzel, P. *Angew. Chem., Int. Ed.* **2006**, *45*, 4651.

(49) Giamello, E.; Sojka, Z.; Che, M.; Zecchina, A. *J. Phys. Chem.* **1986**, *90*, 6084.

(50) Omata, K.; Takada, T.; Kasahara, S.; Yamada, M. *Appl. Catal., A* **1996**, *146*, 255.

(51) Jacobs, J. P.; Maltha, A.; Reintjes, J. G. H.; Drimal, J.; Ponec, V.; Brongersma, H. H. *J. Catal.* **1994**, *147*, 294.

(52) Yu, Y.; Takei, T.; Ohashi, H.; He, H.; Zhang, X.; Haruta, M. *J. Catal.* **2009**, *267*, 121.